PNAS RESEARCH ARTICLE | EVOLUTION ENGINEERING OPEN ACCESS

Microraptor reveals specialized gliding capabilities in multiwinged early paravians

Csaba Hefler[a], Ying Wang[b], Xiaoli Wang[c,d,1], Xiaoting Zheng[c,d], Thomas G. Kaye[e], Maxime Grosmougin[a], Matthieu Chotard[a], Luke Barlow[a], Huihe Qiu[f], T. Alexander Dececchi[g], Michael B. Habib[h], Wei Shyy[f,i], and Michael Pittman[a,1]

Affiliations are included on p. 8.

Edited by Neil Shubin, The University of Chicago, Chicago, IL; received July 8, 2025; accepted December 19, 2025

Agile and efficient modern flyers like birds and insects rely on complex aerodynamics to increase performance such as leading edge vortices, tip vortices, rapid pitch rotations as well as wing–wake and wing–wing interactions. However, their evolutionary origins are poorly understood. Early birds and their closest relatives like *Microraptor* had a multiwinged configuration featuring long pennaceous feathers on their arms, legs, and tail, a configuration not seen today. The skill of these early flyers has been debated, centering around what was driving the evolution of this multiwing configuration and its loss in favor of the modern two-winged configuration. In this context, the aerodynamics and wing–wing interactions of *Microraptor* during gliding flight are investigated. The gliding flight mechanics of *Microraptor* exhibit flow patterns consistent with those observed and quantitatively assessed in volant living animal species. We analyze leading edge vortices on the forewing and hindwing including beneficial wake interactions between them as well as tip vortices on the distinct distally flared hindwing. The latter is unique in *Microraptor* as the hindwing's characteristic outer span flare provides the necessary surface for the tip vortex to be bound to and thus contribute additional lift. These findings suggest that *Microraptor* evolved toward utilizing leading edge and tip vortices and their aerodynamic interactions. This implies that such utilization was also being exploited by other early multiwinged theropods to differing extents as part of a crucial milestone in early flight evolution.

flight evolution | *Microraptor* flight | theropod flight | aerodynamics

Significance

Microraptor was a Cretaceous theropod dinosaur hypothesized to be a glider or a powered flyer. It was unlike any modern flying vertebrate in having a multiwinged flight planform. Here, we investigate the gliding flight of *Microraptor* using updated wing shapes and rigid wing modeling in a conservative forewing and spread leg configuration. This study presents the specific aerodynamic features and associated wing planform specializations of *Microraptor* during different stages of gliding flight. This study provides quantitative estimation of advantageous forewing–hindwing interactions for any multiwinged vertebrate flyer, expanding the scope of animal flight modeling.

The flight characteristics of modern birds, bats, and insects are defined by wing morphology, wing kinematics, and aerodynamic flow conditions (1–7). Birds and bats use asymmetric wing strokes and muscle-controlled morphing to generate unsteady flow patterns enabling efficient flight (4, 5, 8, 9). The smallest flying birds such as hummingbirds as well as insects showcase the most complex unsteady flows including added mass effects, wing bound vortexes, wake capture, and rotational effects as well as the clap-and-fling of the wings in certain insects (4, 5, 9). Finally, wing–wing interactions, as seen in modern dragonflies (5, 10–14), add a whole new level of complexity to flight.

Of all the vertebrate lineages with powered flight, pennaraptoran theropods comprising birds and their close relatives have the best fossil record of early flight evolution. Nonetheless, key questions remain regarding the origins, early evolution, and diversification of pennaraptoran flight. Among the most intriguing and debated features in the early theropod flight record is the emergence and eventual disappearance of five-winged body plans featuring wing surfaces on the forelimbs, hindlimbs, and tail (15). Among the best examples of this morphology is the small, early paravian pennaraptoran *Microraptor* of the Cretaceous Period.

Microraptor had long pennaceous feathers on its arms, legs, and tail (16–18), similar to several other early Mesozoic paravians, but unlike living birds (15). The hindwing functions of *Microraptor* remains contentious: Some investigations have modeled vertical hindwing configurations (17, 19) and recovered evidence for control enhancement during gliding flight (20, 21). Other models use conservatively spread hindwings in gliding flight, resulting in slower flight speeds and differing flight distances (19–26). Estimated flight speeds up to 15 m/s (22, 23, 26) and gliding distances up to 50 to 100 m from a height of 30 m (20, 21, 23) have also been presented as well as lift to drag ratios of 2.5-4 (22, 26) and flight paths with often high local angle of attack (AOA) on the wings for extended times (20, 21, 23). Many early birds including *Archaeopteryx*, *Anchiornis,* and *Sapeornis* had large forewings and smaller hindwings (15) and are usually hypothesized as powered flyers (27, 28), although soaring abilities have been suggested for *Sapeornis* (29, 30) and *Anchiornis* has been proposed as a "borderline" powered flyer (27, 31). Although

Author contributions: C.H., Y.W., T.G.K., and M.P. designed research; C.H., Y.W., X.W., X.Z., T.G.K., M.G., M.C., L.B., and M.P. performed research; X.W., X.Z., T.G.K., and M.P. contributed new reagents/analytic tools; C.H. and M.P. analyzed data; and C.H., Y.W., X.W., X.Z., T.G.K., M.G., M.C., L.B., H.Q., T.A.D., M.B.H., W.S., and M.P. wrote the paper.

The authors declare no competing interest.

This article is a PNAS Direct Submission.

[1]To whom correspondence may be addressed. Email: wangxiaoli@lyu.edu.cn or mpittman@cuhk.edu.hk.

This article contains supporting information online at https://www.pnas.org/lookup/suppl/doi:10.1073/pnas.2518106123/-/DCSupplemental.

Published January 26, 2026.

recent work suggests that *Microraptor* was capable of powered flight (27, 32–34), the duration and specific performance of this powered flight is still unclear. The foundational work to understand its powered flight dynamics necessitates in depth study of the simpler case where both the forewings and hindwings are in a fixed position. Previous work has not presented detailed flow structure analyses or evaluated the role and mechanisms of possible wing–wing interactions in the flight of any early pennaraptoran flyer, including *Microraptor*. Thus, given that a fixed wing scenario is a helpful starting point and that powered flyers use gliding phases, here we model a fixed-wing wake interaction scenario during glides in the low, moderate, and high AOA flight regimes.

Inherent wing–wing and wake interactions are known in insects and migratory birds (35–38). These are particularly well documented in dragonflies which can individually control each of their wings (39), permitting versatile utilization of downwash effects and vortex interactions (5, 35, 40–42). When the forewing interacts with the incoming flow, which is faced by the hindwing, a downwash effect typically results. On the other hand, the forewing also sheds vortices in its wake that results in interwing flow patterns which vary according to flapping specifics as well as spanwise location along the wings. Depending on wing phasing and flight speed, these interactions can be beneficial or detrimental to flight efficiency. During forewing-led wing phasing, downwash attenuates hindwing leading edge vortex (LEV) circulation (43). During hindwing-led wing phasing, hovering with all four wings consumes ~22% less power than with just two wings (44). Their forewing can also shed a trailing edge vortex (TEV) promoting formation of the hindwing LEV (43, 45), due to partial vortex fusion (46). The forewing TEV and hindwing LEV interact synergistically if they form in close proximity (47, 48). These wing–wing interaction insights from modern dragonflies and other living animals provide a framework to investigate the utilization of wing–wing interaction in ancient fliers, especially those with broadly similar sizes living under comparable environmental conditions.

Here, first-principle Navier–Stokes equation–based numerical investigations (49) of the aerodynamics and forewing–hindwing interactions of *Microraptor* are used to characterize wake elements and their benefits to flight to expand our understanding of early theropod flight evolution. To do so, this study makes use of the latest anatomical insights integrated from over 100 fossilized specimens of *Microraptor*, including wing profile and body outline information only observed under laser-stimulated fluorescence (LSF) (34, 50–52).

Results

Gliding Flight Scenarios. In this study, we investigate the aerodynamic features of the gliding flight of *Microraptor* in the low, moderate, and high AOA flight regimes. The AOA is the angle between the body axis of *Microraptor* and the direction of the incoming flow, and it is fixed at 2° and 10° lower than the AOA of the forewing and the hindwing, respectively, according to the preset pitch of the wings in the modeled flight gait. In our setup, we vary the AOA from 0° to 30° in 3° increments in addition to 45° and 60°, mimicking a series of wind-tunnel experiments. The calculated glide angles (see Supporting Information, SI) of the resulting aerodynamic forces indicate a steeper flight path than this preset AOA, which can be attributed to the simplifications in our model (details given in the Methodology and *SI Appendix*). We use the Q-Criterion to help highlight coherent vortical structures within the flow field where the vorticity magnitude is greater than the magnitude of the rate of strain:

$$Q = -1/2\left(0.5S^2 - 0.5\omega^2\right) \quad [1]$$

where S is the shear strain rate, and ω is the vorticity.

Evident from the streamlines and the isosurfaces of the Q-criterion (1) in Figs. 1 and 2, that in the low AOA flight regime (0° to 12° in Fig. 1) the flow around the wings remains attached, and the wings operate in some respects as a modern slotted wing would: The leading airfoil creates a downwash that channels the flow above the trailing airfoil limiting flow separation on it (Fig. 2 *A*–*F*). For both wings, the LEV is first insignificant (and limited by the downwash effect in the hindwing) and then it gradually becomes more prominent as the AOA increases. On the outer span of the hindwing, where the gap separating the wings is larger, the downwash is weaker. This and the preset pitch angle of the hindwing result in a local AOA that allows the formation of a tip vortex (Fig. 2 *A* and *C*). This tip vortex extends downstream along and above the distinct distally flared outer span of the hindwing (due to the hindwing's shape with the outer portion substantially tilted downstream, it is somewhere between a straight and delta wing, and hence, the resulting vortex flows). This vortex is bound to the extended lifting surface provided by the outer span flare of the hindwing, thus, it contributes to lift generation substantially more than if the wing tip was narrower (4, 53–55). In a sense, the tip vortex of the hindwing of *Microraptor* can be thought of as an elongated LEV with a downstream orientation utilized with the help of the specialized shape of the hindwing. No such tip vortex is formed on the forewing.

Fig. 1 shows the total (forewing and hindwing) force coefficient of lift (2) and drag (3) (see *SI Appendix* for additional details).

$$C_L = L/qA \quad [2]$$

$$C_D = D/qA \quad [3]$$

where L and D are the lift and drag forces, A is the area of the forewing (0.02191 m^2), and $q = (\rho U^2/2)$ is the dynamic pressure, with ρ the air density (1.225 kg/m^3) and U the airspeed (10 m/s in Fig. 1). Please note that the forewing planform area is used as the reference area for all of the force coefficient calculations. Lift is perpendicular to the direction of flight and drag is parallel with it. In gliding, lift provides the vast majority of weight support, while drag primarily opposes the forward motion, and thus a higher lift to drag ratio results in a longer glide distance for a given sink distance. In the low AOA regime, the force coefficients increase quasi-linearly and the slope of the lift is steeper than that of the drag. The levels of lift to drag ratio are comparable to values reported in other works (22, 26).

In the moderate AOA flight regime (12° to 30° in Fig. 1), bound leading edge vortices are observed on the forewing and hindwing (*SI Appendix*, Fig. S1). A wing bound vortex on the upper surface of the wing contributes to force generation in two ways. The vortex maintains a low-pressure core that lifts the wing (4, 53–56). Second, the vortex induced flow helps flow reattachment (delaying stall) and momentum transfer to the surrounding air (4, 53–56). The role of these vortices in *Microraptor*'s wing–wing interactions is strong, resulting in a substantial and sustained lift boost. Furthermore, within the moderate AOA regime, the lift reaches a plateau and the total lift peaks close to 30° (where C_L is 1.83), while the drag keeps increasing gradually and the lift to drag ratio decreases accordingly.

In the high AOA flight regime (above 30° in Fig. 1), first the forewing and then both sets of wings experience vortex detachment that results in flow separation. This leads to the loss of lift while drag increases, as seen in Fig. 1. Critically stalled flow makes flight unsustainable for more than a very brief interval. Such flow conditions are minimized in living birds by spanwise variation of the wings AOA (4), but it is unclear whether early flyers like

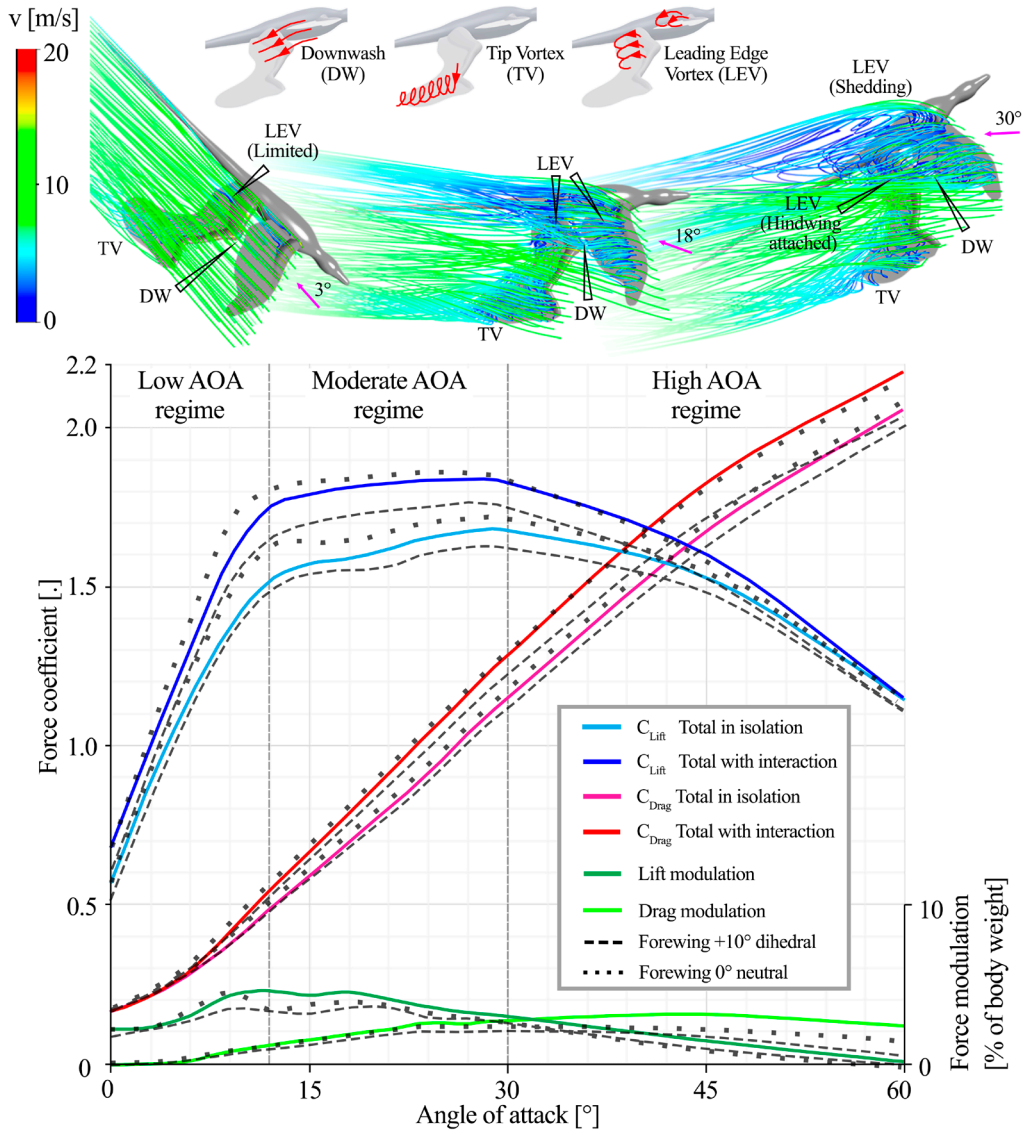

Fig. 1. Flow characteristics in different flight regimes of *Microraptor*. Models with 10 m/s flight speed in the low, moderate, and high AOA flight regimes (interpreted as a steep glide, glide of moderate descent and a hypothetical landing approach). Flow patterns in representative cases (forewing in anhedral position) of 3°, 18°, and 30° AOA (indicated by purple arrows) visualized by streamlines colored according to velocity magnitude. Total force coefficients of the wings with and without interaction, and total lift and drag modulation expressed as a percentage of the 0.68 kg estimated mass of *Microraptor* (the same plots of neutral and dihedral forewing setup are marked with black dashed lines). These flight conditions were simulated in sequence, but this does not necessarily represent a true flight path.

Microraptor could do something similar. Nevertheless, these flow conditions are present when modern birds land and during brief and extreme flight maneuvers (4). Overall, we can interpret the corresponding flight scenarios in the low, moderate, and high AOA regimes as a steep glide (or aerial dive), moderate descent, and as a hypothetical landing approach, respectively.

Fig. 2 shows the hindwing (Fig. 2 *A* and *C*) and forewing (Fig. 2 *E* and *G*) flow patterns in detail in flight with both fore- and hindwings modeled as well as in the hypothetical case of the hindwing (Fig. 2 *B* and *D*) and forewing (Fig. 2 *F* and *H*) modeled in isolation for a representative low AOA regime flight (3° AOA). The streamlines and isosurfaces confirm that the flow is attached to the forewing and slightly deflected downstream, causing downwash effects on the hindwing (Fig. 2 *A–D*). The nearly identical isosurfaces and streamlines in both cases indicate that the presence of the hindwing only marginally affects the flow dynamics of the forewing (Fig. 2 *E–H*), and the same can be said for the moderate and high AOA regimes (*SI Appendix*). In *SI Appendix*, all the flow features discussed above are shown in a representative case of a moderate and a high AOA regime flight, respectively, in the same format as in Fig. 2.

Additionally, in Fig. 1, the force coefficients with the forewing in a neutral 0° and +10° dihedral position are also plotted in comparison to the -10° anhedral forewing setup. In a neutral position, lift increased with a slight increase of drag in the 3° to 30° range, but both decrease for larger angles of attack. In the dihedral position of the forewing, both lift and drag decrease for all the investigated flight regimes, with lift being slightly more affected, showing that the dihedral forewing position in a tandem gliding setup may be more for flight stability reasons [as seen with gliding birds and in aircraft design (4, 57)] then to maximize aerodynamic efficiency.

Force Modulation Due to Forewing–Hindwing Flow Interaction and the Effect of Flight Speed. Fig. 1 shows the coefficients of total lift and total drag in interaction and with the wings in

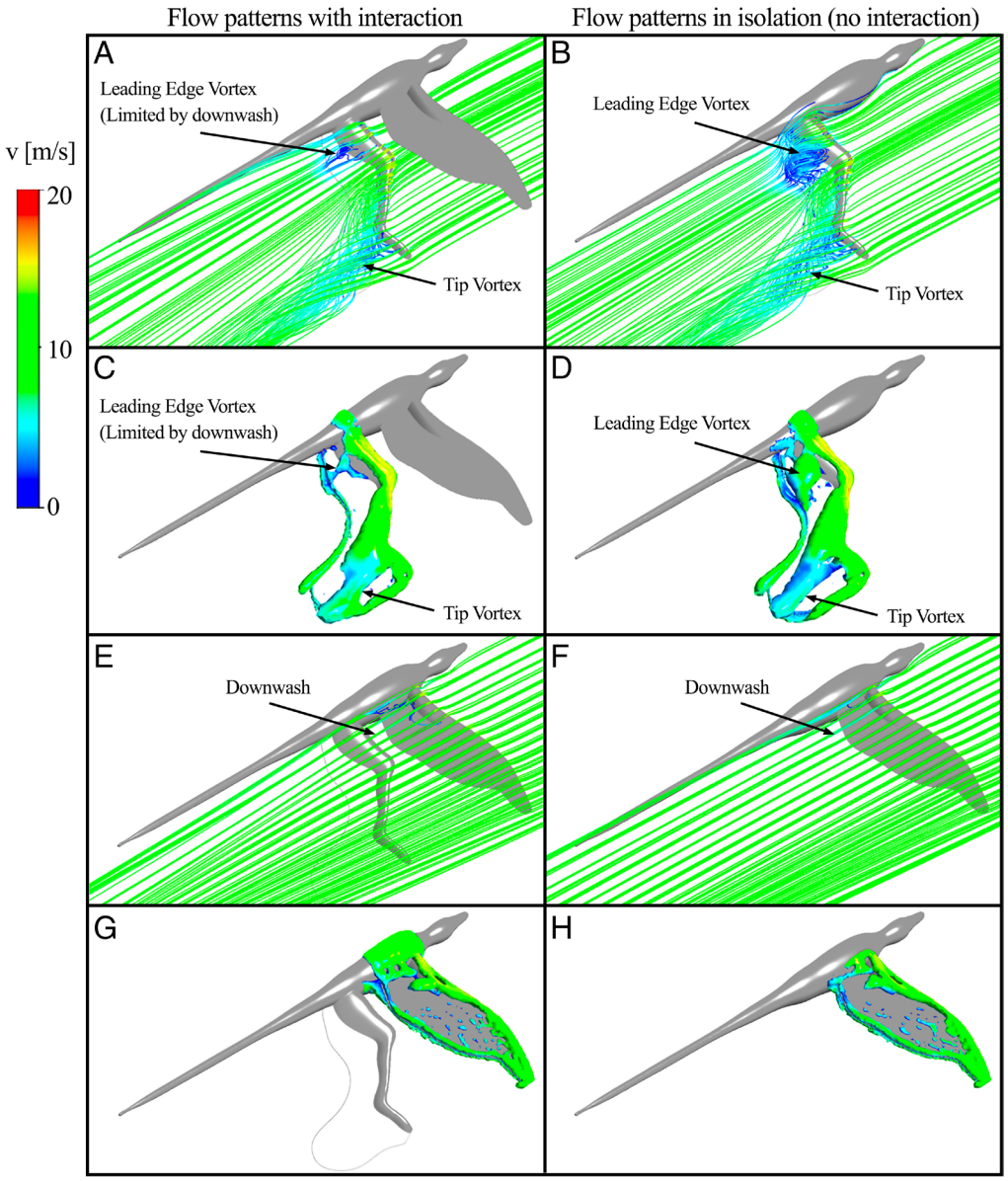

Fig. 2. (*A*–*H*) Flow characteristics in the low AOA flight regime of *Microraptor* (3° AOA, 10 m/s glide speed). Streamlines (*A*, *B*, *E*, and *F*) and isosurfaces of the Q-criterion of 9000 $1/s^2$ (*C*, *D*, *G*, and *H*) of the hindwing and the forewing (in anhedral position) in flight with two wings (*A*, *C*, *E*, and *G*) and in the hypothetical case of each wing in isolation (*B*, *D*, *F*, and *H*). Streamlines and isosurfaces are colored according to flow speed.

isolation for 10 m/s flight speed. From this, the total lift and drag modulation can be calculated by subtracting the total lift or drag of the wings operating in isolation from the total lift or drag of the wings with interactions involved to quantitatively present the forewing–hindwing interaction. The latter is also shown in Fig. 1 as a percentage of the estimated mass of *Microraptor* (22, 23) used in this study (0.68 kg). Within the probably flight speed (23) range modeled for *Microraptor* (5 to 15 m/s), the lift to drag modulation ratio remains nearly constant, and so does the presented flow characteristics (*SI Appendix*). In this section, we present the results regarding a glide speed of 10 m/s and the forewing in an anhedral setup (values for 5 and 15 m/s are given in *SI Appendix*). Although the drag is increased by the interaction, the lift boost is more substantial for flight before stall develops. The total lift increases over 4% of weight in the 9° to 21° AOA range, reaching a maximum of 4.6% at 12° (Fig. 1). The drag decreases below 6° and increases smoothly above 6°, but remains less than the lift modulation below 30°. The maximum drag increase occurs at ~45°, where it is still only 3.1% of the estimated weight.

With the forewing in neutral and dihedral positions, the interaction effect weakens as the physical distance between the wings increases (Fig. 1). The drag modulation gradually lessens toward larger angles of attack. The lift modulation on the other hand decreases similarly for both the neutral and dihedral setups above 21°, while the neutral setup outperforms both the anhedral and dihedral setups below 9°, although this is marginal in comparison to the anhedral setup. For above 9° and in the moderate AOA regime, the lift modulation decreases proportional to how the forewing becomes more removed from the hindwing in the neutral and anhedral setup, pointing to the importance of the interaction effect in lift.

Flight Stability. During gliding, an animal experiences two primary forces: the total aerodynamic force acting at the center of pressure and its weight acting at the center of gravity. The surface pressure zones (*SI Appendix*) are a manifestation of the local aerodynamic forces which the animal can control via active wing morphology. Integrating the surface pressure gives the center of

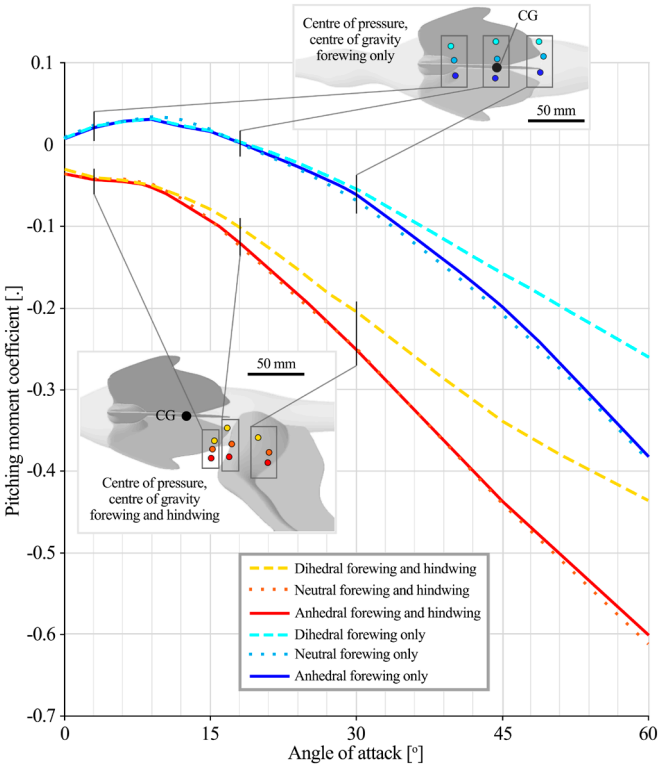

Fig. 3. Pitching moment coefficient in 10 m/s gliding flight with different wing configurations. The center of pressure and estimated center of gravity (CG) in a given low AOA regime glide (3°), moderate AOA regime glide (18°) and high AOA hypothetical landing approach (30°) are shown graphically as well.

pressure (Fig. 3). Depending on the distance between the center of pressure and center of gravity, the total aerodynamic force introduces a moment (M) to the center of gravity. The smaller the absolute value of this moment, the closer the glide is to an equilibrium state. Based on anatomical descriptions (16, 17), the center of gravity in *Microraptor* was previously estimated to be near the centerline of the body and ~0.9 forewing mean chord length behind the leading edge of the forewing (20). Thus, in a similar fashion, we define the center of gravity (Fig. 3) to be in the centerline of the body 71 mm behind the leading edge at the wing root that is 197 mm from the tip of the head (the mean chord of the forewing of our model is 78 mm).

Passive stability requires static stability ($\partial M/\partial\alpha < 0$ over a range of α, where α is the AOA) and, secondarily, dynamic stability, though the latter can often be mitigated through moderate active control of the lifting surfaces. In natural flight, the response rate of active control in pitch is more demanding in comparison with yaw, in which case wing shapes alone grant sufficient static stability (58). Accordingly, to assess flight stability in the studied glide scenarios, we calculated the moment coefficient of pitch for 10 m/s glide speed (Fig. 3):

$$C_M = M_p / qAL \quad [4]$$

where M_p is the pitching moment, and L is the body length of *Microraptor* (0.7 m). A positive moment results in nose up pitching, and if $\partial C_M/\partial\alpha$ is negative, zero, or positive, the flight is stable, neutrally stable or unstable. Accordingly, in Fig. 3, we plot C_M as a function of the AOA, in which case the local slope is indicative of flight stability. Our model does not include the tail feathers as the fifth aerodynamic surface of the *Microraptor* flight planform, but assuming that the tail plays an important role in stabilizing pitch during gliding flight (59), we can hypothesize its elevated or depressed position during the investigated flight scenarios. In Fig. 3, we show the center of pressures and moment coefficients for the three distinct glide scenarios. In Fig. 3, we also added the hypothetical case of including only the forewings, this case can be considered analogous to *Microraptor* flying with its legs down using them for additional yaw and roll authority (20, 21). For all of the cases plotted, positive pitching moments indicate that some combination of forewing rear sweep and/or upward force (positive lift) from the tail would be correcting, while negative pitching moments would be corrected by some combination of forewing forward sweep and/or downward force (negative lift) producing tail positions. For forewing only configurations, there are some cases where a small amount of rear sweep is implied. For all other cases, variable amounts of forward sweep are implied.

Discussion

Our results show that for a range of realistic speeds, a conservative range of wing posture estimates, and a wide range of flow conditions, *Microraptor* could utilize distinct aerodynamic effects as well as forewing–hindwing interactions and their resulting aerodynamic force modulations.

The hindlimb as a second wing is an intriguing feature of *Microraptor*. However, its reduced ability to pitch due to lower hip mobility (25) would induce drag that would reduce speed gain during low AOA steep glides. This drawback is largely negated in the wake of the forewing downwash, as seen by the streamlined flow around the hindwing in Fig. 2*A*. Arguably, the hindwing in the spread leg, forewing–hindwing arrangement is a net positive feature even in low AOA glides, despite the physiological limitations of the hip joint. We must note that the spreaded leg flight configuration is just one possibility for *Microraptor*. Previous studies evaluated flight with a hindwing down posture in which the legs may function as a kind of rudder for flight control (20, 21). With the added possibility of flapping the forewings and positioning the hindwings anywhere from a spreaded leg configuration to a completely legs down posture, *Microraptor* could adapt well to possible flight scenarios, and it is an aspect that should be further studied.

Gliding in the moderate AOA flight regime is characterized by a LEV and tip vortex flow patterns. Both vortices are bound to the surface of their respective wings, thus, contributing to aerodynamic force generation not only by preserving a low-pressure region and delaying stall but also by partaking in mutually beneficial aerodynamic interaction between the wings. Substantial force gain by the aerodynamic interaction is present and almost invariant in the full range of flight speeds and directions in this flight regime (Fig. 1). For the 10 m/s flight speed case with anhedral forewing positioning, the maximum lift coefficient amplification was found at 12° AOA to be 0.23 accounting for about 4.6% of the estimated bodyweight of *Microraptor* (for reference, the drag coefficient only increased at 12° by 0.06 that is about 1.2% of the estimated bodyweight). This confirms that the wing bound vortices characterizing this phase are helping to maintain high lift (4, 53–55). These beneficial flow features of the forewing–hindwing configuration of *Microraptor* are present in a wide range of flight directions; essentially in the complete moderate (and partly in the low and the high) AOA flight regime. Interactions are also present for neutral and dihedral forewing positioning, although to a lesser extent, showing that the kinematic-morphologic adaptations for the utilization of these aerodynamic effects is generally advantageous for multiwinged early paravian flyers. Wake interaction effects that enhance lift production implicitly improve weight support and/or thrust

generation for the same mechanical power input. Since the relatively smaller flight muscle fraction of early theropod flyers like *Microraptor* probably made them power-limited in flight, the wake interaction effects identified here would necessarily have enhanced powered flight too by reducing power requirements.

Fig. 3 presents how the center of pressure and the resulting pitching moments vary with different wing configurations in the investigated flight cases of *Microraptor*. The hypothetical forewing only case is more stable in the investigated angles of attack range, agreeing with previous findings (21) (drag of the hindwings in a perfectly aligned legs down configuration would cause some negative pitch that is not considered in this hypothetical setup). In the low and partly in the moderate AOA regime (between 0° and 18°) the pitching moment is positive. Beyond 18° it becomes progressively more negative, indicating that the flyer stays statically stable and experiences restoring moments making it more difficult to maneuver.

The hindwings in the spread leg posture move the center of pressure backward, resulting in an increased negative pitch moment that would presumably be corrected by a combination of forward sweep of the forewings and/or elevation of the tail. An elevated position of the feathered tail by *Microraptor* seems to help achieve stability in pitch when the hindwings are spread. Finally, the configurations with anhedral and neutral positioning of the forewing result in nearly the same pitching moments, while the moments are substantially reduced in the dihedral forewing position. This shows that the forewing in a dihedral position improves stability, although wing sweep and deployment of the tail would still be necessary to increase flight stability and provide efficient flight control, especially when AOA becomes larger.

Most interestingly, in the given spread leg position, the leading edge of the outer half span of the hindwing gradually feeds a well-defined tip vortex that follows the extended wing area provided by the especially long primaries of the feet. This vortex generates aerodynamic force even at lower angles of attack. The specific posterodistal expansion of the hindwing planform which coincides with the path of this tip vortex suggests a marked evolutionary specialization of *Microraptor* to its utilization. In comparison, other multiwinged early paravians, including the early birds *Archaeopteryx* and *Anchiornis* (15), lack this expansion preventing them from utilizing the tip vortex as effectively. Furthermore, from *Microraptor* (51) and from *Anchiornis* (60) and *Archaeopteryx* (61, 62) toward later fossil birds such as *Sapeornis* (30), there is a general pattern of distal to proximal reduction in hindwing feathers (15, 51), highlighting functional changes of the hindlimbs as these species became more capable powered flyers. However, in the following hypothetical we consider the possible gliding and soaring flight of these other species to give more context for the flight of early multiwinged flyers. *Anchiornis* and *Sapeornis* possess remarkably similar hindlimb feathering having longer pennaceous feathers at the tibial and metatarsal sections of their legs forming a small aileron-like winglet on their leg (15). The relatively narrower leg winglet and the more slender wings of *Sapeornis* (30) may be suggestive of soaring adaptations. Soaring specialization tends to optimize energy extraction efficiency, leading to drag reducing planforms. Reducing drag (by reducing the profile and streamlining the hindlimbs) might then have been more important than steep turns or additional lift generated by the hindwing. This partially explains why the hindlimb feathers of *Sapeornis* are shorter and function more as a streamlining apparatus than a flight control surface. This differs from *Anchiornis* (and *Archaeopteryx*) which had a comparatively more expanded hindlimb wing area that could potentially be used as a yaw and roll generator in flight to provide more control for maneuvering and obstacle avoidance. The relatively smaller hindwings of *Anchiornis*, *Archaeopteryx,* and *Sapeornis* compared to *Microraptor* could still be an effective lifting surface if needed. In doing so, we can hypothesize the inherent leading edge and tip vortexes to be present, but with comparatively more limited interaction between the wings, primarily via downwash. The tibial winglet of *Anchiornis* and *Sapeornis* in particular may have produced a horseshoe-like vortex structure forming an inner and an outer tip vortex pair. We have not considered the role of tail here, but we do also note that *Microraptor* possesses a particularly long, stiffened tail and that the tail fans of microraptorans have been previously assessed (quantitatively) as having performance-enhancing control properties, especially in pitch (59). The anatomies of more modern animals, like *Sapeornis*, represent reductions in the pitching moment arm and/or lifting area of the tail, in addition to their aforementioned reduction of hind limb feather surfaces. Taken with our hindwing modeling results, this produces an overall theme of greater reliance on nonforewing control and/or weight support in more stemward taxa, with reduced reliance on such surfaces (with concomitant reliance on more sophisticated and robust forewings) in more crownward taxa. Thus, our study significantly expands the scope of flight experimentation undertaken by early theropod flyers (63).

Conclusion

Here, we show qualitatively and quantitatively that *Microraptor* could have utilized aerodynamic features similar to what is seen in modern birds, for a range of conditions that are realistic given current knowledge. This pushes back the presence of these sophisticated flight dynamics to the Early Cretaceous. In addition, we demonstrate the potential for beneficial interactions between the forewing and hindwing. Wing–wing interactions are commonly seen in other multiwinged flyers and there is a substantial and growing literature on the topic (5, 10, 11, 13, 14, 64). The current study adds more insight into the rich physics related to the aerodynamics of wing–wing interactions. In the context of the similar body plans of the other multiwinged early paravians of the Late Jurassic and Early Cretaceous, our results suggest that greater utilization of unsteady aerodynamic features was potentially a crucial milestone of early flight development.

Some of the features returned in our simulation (such as sustained leading edge vortices) are known in modern birds (4, 65, 67, 68). However, the specialization of the hindwing to accommodate the downstream extended tip vortex for a wide range of angles of attack is to our knowledge unique among flying animals, including four-winged insects. This unexpectedly robust feature with the help of wing–wing interactions may have permitted *Microraptor* to experiment more broadly with flight using different wing configurations, especially for the forewing, that could have helped this species transition to powered flight, whose potential was previously proposed (27). We therefore propose *Microraptor* as a model species to demonstrate the utilization of further complex aerodynamic effects in the evolution of modern flapping flight. In summary, this study breaks ground in understanding the origins of the utilization of wing bound vortexes and interwing aerodynamic effects elucidating what was behind the development and eventual extinction of multiwinged flight configurations in early birds and their close relatives as well as what enabled powered flight to develop as we know it today.

Materials and Methods

3D Model. Landmarks of the humerus, ulna, metacarpal, femur, tibia, and metatarsus as well as the shoulder joint-body centerline distance, hip joint-body centerline distance and the shoulder-hip distance were recorded from

well-preserved specimens of *Microraptor* (IVPP V13320 and V13352; STM 5-5, 5-93, 5-142, 5-150, 5-172, and 5-221) to create a complete skeletal frame that was sized to the average humeral length of the specimens studied (see SI). Body and feathering contours as preserved in the fossilized remains under white light and LSF were scaled and then fixed as solid bodies to this skeletal frame. These contours move together with the parts of the skeletal frame as the angles at the joints are set. The resulting outline is the final planform of the wing that is used to construct the wing surface. The aerodynamic surface of the wing feathering was simplified in the numerical model as a 1 mm thick rigid flat plate with rounded edges. Natural feathers are flexible, and it has been shown that the flexibility of the wings improves flight performance to some extent [delaying stall, improving aerodynamic stability, and force generation (4, 5, 8, 9)]. Considering this, our modeling provides a lower-bound approach to the flight capabilities of *Microraptor*, while the discussed findings regarding the characteristic aerodynamic patterns and importance of wing–wing interactions can be safely assumed to be valid regardless of flexibility.

Forewing feathering was reconstructed with the primary feathers (STM 5-9 and BMNHC PH881), secondary feathers (IVPP V13352), greater coverts (STM 5-93 and 5-221), median coverts (STM 5-5 and 5-109), and marginal coverts (STM 5-109) following the most recent reconstruction (52). Feather count within each feather series was inferred using comparisons with modern bird feathering patterns (52). Our forewing reconstruction of *Microraptor* shows a more extended wing (larger humerus-forearm and forearm-manus angles) like the reconstruction of Chatterjee and Templin (23). Our reconstruction maintains the long and extended wing tip of previous reconstructions created by the long primary remiges (17, 20, 23), but unlike previous work (17, 20, 23), our reconstructed wing tip has a slenderer V-shape. Unlike previous work (17, 20, 23), the length transition between primary and secondary feathers is sharper, creating a deep and narrow notch between them. The secondary feathers also gradually decrease in size proximally along the forearm, creating a relatively straight trailing edge, that is at the same level as the trailing edge of the primary feathers (52).

Hindwing feathering was reconstructed with metatarsal remiges (STM 5-75 and 6-86; BMNHC PH881), long metatarsal coverts (STM 5-5 and 5-75), anterior coverts (STM 6-62 and 6-86), short coverts (STM 5-5, 5-75 and 6-86), long tibial feathers (STM 6-86), and long femoral feathers (STM 6-86) following the most recent reconstruction (51). The number of feathers within a given feather series was directly counted or inferred by estimating the number of missing feathers using the width and length of the preserved feathers in the series. Our revised hindwing reconstruction follows the one of Chotard et al. (51) and has a more distally shifted subtriangular trailing edge shape with its apex at the approximate level of the ankle joint. The proximal edge of this subtriangular shape is formed by the tips of the primary remiges closest to the apex; the edge is then indented and formed by the tips of the tibial feathers furthest from the apex. The distal edge is formed by the tips of the primary remiges only.

Soft tissue of the forewings and hindwings were modeled by a loft surface defined by symmetric NACA blade profiles (and a combined blade profile at the elbow to account for the propatagium) fixed to the skeletal frame. The chord of these NACA profiles were defined using the soft tissue preserved in fossil specimens STM 5-93 and 5-221 for the forewing as in ref. 52 and specimens STM 5-5 and 6-86 for the hindwing as in ref. 51. The chord to thickness ratio of the NACA profiles were defined according to the ratio of modern birds that are behavioral short distance flyers (chickens). Specimen STM 5-93 and 5-221 shows a well-preserved propatagium of *Microraptor* (34) although the forewing is not extended as it would be during flight. Thus, to estimate the propatagium thickness in the modeled flight gait with a 145° elbow angle (Fig. 4) we used a linear extrapolation. Further details are provided in the SI.

It is known that a thinner, cambered, and flexible wing will yield better aerodynamic performance (4, 5, 8, 69, 70). However, there is a lack of data regarding the *Microraptor* wings' cross-sectional shapes and structural flexibility. Here, we offer a conservative assessment choosing a nonflapping, rigid wing with a symmetric airfoil profile in steady state wing positions with varied AOA, and fixed fore- and hind-wing arrangements. Such an approach yields a lower-bound evaluation regarding *Microraptor*'s airborne capabilities.

The body contours were modeled using the reconstruction made in ref. 34 that is based on IVPP V13352. We simplified the body contours in this study as an axisymmetric rigid body defined by the ipsilateral dimension along the body axis as its diameter. Tail feathering and its aerodynamic effects are outside the scope of this study; thus, no lifting surface modeling of tail feathers were combined with the body model. The dimensions of the model are shown in Fig. 4. Early paravian flyers, including *Microraptor*, had a relatively laterally orientated shoulder joint that facilitated a range of arm motion (27, 34, 71, 72), but wing position during gliding flight remains unclear in the absence of ligamentous (and other soft tissue) constraints of shoulder mobility [sensu (25)]. When modern birds glide, larger species tend to hold their wings in dihedral positions, while smaller species tend to hold them in anhedral positions (57, 7374, 75). Thus, to take both of these aspects into consideration, our modeling covers a conservative range of forewing positions: −10° anhedral, 0° neutral as well as 10° dihedral (also includes previously modeled positions: seemingly 0° in refs. 20, 21, 23, and 26 and ~2° to 10° in ref. 22). As wing–wing interactions are expected to be the strongest when the forewings and hindwings are closest together, the −10° anhedral position of the forewing (Fig. 4) was selected as the reference case with the 0° neutral and 10° dihedral cases discussed in the context of it (*SI Appendix*, Fig. S1).

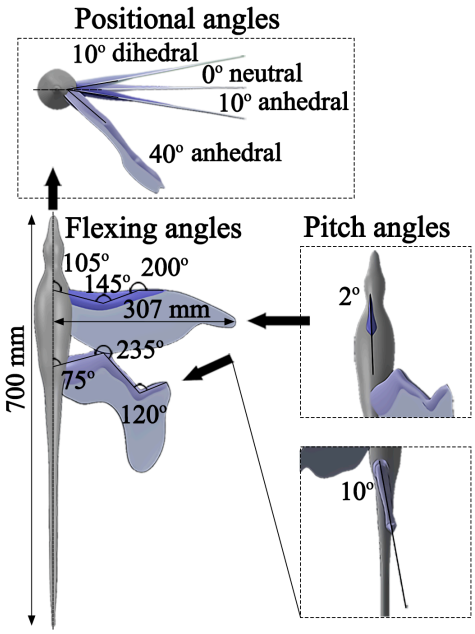

Fig. 4. Main dimensions of the 3D model of *Microraptor* in a conservatively spreaded leg configuration.

The ability of microraptorines to sprawl their hind limbs is contentious. It is widely agreed that extensive abduction of the hips was not possible for most theropods, and living theropods (i.e., birds) have limited abduction range of motion. This is underscored by range of motion mapping of ligamentous constraints on modern avian hip mobility that was used to recommend more conservative hip mobility for extinct ornithodirans compared to previous work, including for *Microraptor* (25).The authors provided a range of hip motion "morphospace" that summarized their results. We have taken our maximum abduction range from the center of that morphospace. Thus, our 40° anhedral angle spread leg configuration is therefore both conservative and well-supported by the combination of hard and soft tissue evidence currently available. The angles defining the gait are shown in Fig. 4.

Sensitivity to 3D Model Positioning. Considering the reported findings of this work and the significant computational effort behind it, it is still important to briefly discuss the sensitivity of the results to moderate changes in 3D model positioning. Moderate changes of the anhedral angle would not fundamentally change the conclusions made. A larger angle separating the forewings and hindwings would make downwash and interaction effects less prominent to the point where little or no interaction would prevail in the case of a vertical legs down configuration. A larger anhedral angle would also orient the total force vector of the wing (forewings and hindwings likewise) outward, away from the flight direction reducing lift. The wing flexing angles delineate the size of the lifting surface of the wings and thus fundamentally define the overall aerodynamic force

generation; small changes of the assumed angles however would not affect the reported findings qualitatively. Finally, the pitch angle of the wings affects the local AOA of the wings. Higher AOA results in an earlier onset of dynamic stall (followed by static stall). In case the pitch of the forewing or the hindwing is adjusted individually, the flight angle where the reported flow features appear would shift accordingly, but within a reasonable range of pitch angle change, the qualitative features reported in this work would not change.

Flow Fields and Wake Calculation. To solve the flow field in this work, the viscous shear stress transport (SST k-ω) turbulence model with low-Reynolds corrections was used in the commercial solver *Fluent 2023 R1* (49). Reynolds number describes the relative importance of inertial forces vs. viscous forces in a fluid flow. Low Reynolds number corresponds to stronger viscous forces (76, 77). The computational domain used in this study consists of two zones. A fine mesh zone near the studied model extends 1 body length (BL) in depth (about 1.16 of the forewing tip to tip wingspan in our configuration) from the centerline of the body, 2 BL to the top and the bottom from the centerline of the body, 2 BL downstream from the tip of the tail, and 0.1 BL upstream from the tip of the head. Similarly, a coarser mesh outer zone extends 1.7 BL in depth (about 2 of the forewing tip to tip wingspan in our configuration) from the centerline of the body, 5 BL to the top and bottom from the centerline of the body, 5 BL downstream from the tip of the tail, and 2 BL upstream from the tip of the head. The boundary conditions were set as follows. A symmetry boundary condition was set through the midplane of the body. The inlet, top, bottom, and the side of the domain were defined as velocity inlets with the x and y components of the velocity defined according to the flight speed and direction. The outflow was configured as a pressure outlet. The surface of *Microraptor* was set to be a slip-free wall. With the help of the inbuilt meshing software of *Ansys Workbench 2023 R1* (78), the mesh was created to have maximum element sizes of 40 mm at the outer edge of the outer zone, transitioning to maximum element sizes of 10 mm at the edge of the fine region, that further reduces to a maximum element size of 3 mm at the faces of the *Microraptor* model. All elements are in the quadratic order resulting in more than 15 million nodes and 10.5 million elements within the computational domain. In the final step, this mesh was converted to a polyhedral mesh for added precision. A grid independence study was carried out to show that the quality of the mesh was sufficient (*SI Appendix*). With the above setup, after an automatic initialization, less than 200 iterations resulted in convergence of the residuals.

Reference Values. We used the following reference values consistently. The fluid in the domain was air (constant density 1.225 [kg/m^3]; constant viscosity 1.7894 × 10^{-5} [kg/m*s]). Reference area is the planform area of the forewing that is 0.02191 m^2. Reference length is the average chord length of the forewing 0.078 m. Reference velocity is the flight speed 5, 10, and 15 m/s, respectively. Our modern-day-based reference value for air density is appropriate as it roughly mid-way between the highest (1.35 kg/m^3) and lowest (1.17 kg/m^3) estimates for air density using differing methodologies (79, 82, 83) during the Early Cretaceous when *Microraptor* lived (~130 to 110 Mya). However, for completeness, we consider the implications of the highest and lowest estimates of air density on the Reynolds number range in our modeling. The lowest Reynolds number is 2.56 × 10^4 for the lowest air density estimate at the lowest flight speed considered (5 m/s) compared to 2.68 × 10^4 when modern air density is used instead. The highest Reynolds number is 8.86 × 10^4 for the highest air density estimate at the highest flight speed considered (15 m/s) compared to 8.04 × 10^4 when modern air density is used instead. This difference in Reynolds number range only equates to a slightly widened speed range of 4.7 m/s to 16.5 m/s using modern air density. As detailed in the discussion (see also in SI), flight speed (or Reynolds number) has little effect on flow interaction and the presented flow patterns in the investigated Reynolds number range.

Isolating the Wing–Wing Interaction Effect. Calculation of the force coefficients was made with and without the effect of wing–wing interaction. The numerical simulation was run for four models of *Microraptor*: Model 1, body only; Model 2, body and forewing ensemble; Model 3, body and hindwing ensemble; Model 4, body, forewing, and hindwing ensemble. The body and forewing ensemble model (Model 2) together with the body and hindwing ensemble model (Model 3) were used to calculate the force coefficients without wing–wing interaction effects. The body, forewing, and hindwing ensemble model (Model 4) was used to calculate the coefficients with interactions involved. The force coefficients calculated using the body only model (Model 1, without any of the wings) were subtracted from both the with and without wing–wing interaction cases for the discussion of the aerodynamics of the wings (we assumed that the body forces were the same in both cases).

LSF. LSF imaging (84) involved scanning a 405-nm violet laser line over the specimens in a darkened room. The source was a laser diode projected through a line lens. Long exposure photographs were taken over 30-s exposures with a Nikon DSLR camera fitted with a 425-nm laser blocking filter. LSF photographs were postprocessed across the full frame of the image in *Adobe Photoshop CS6* for equalization, saturation, and color balance.

Data, Materials, and Software Availability. All study data are included in the article and/or *SI Appendix*.

ACKNOWLEDGMENTS. We thank the staff of the Shandong Tianyu Museum of Nature for their support during specimen study. We thank the attendees of the Theropod Flight Origins Symposium of the 2023 Society of Vertebrate Paleontology Annual Meeting and the 2nd and 3rd International Pennaraptoran Dinosaur Symposium (IPDS2 and IPDS3) in 2022 and 2024 for their supportive feedback. This project was supported by the Research Grant Council of Hong Kong's General Research Fund (17105221 and 14116623 to M.P.) and the School of Life Sciences, The Chinese University of Hong Kong, including the postdoctoral fellowship of C.H., the research assistantships and PhD studentships of M.G. and M.C., and the research assistantship of L.B. X.W. and X.Z. were also supported by the Taishan Scholars Programme of Shandong Province (Ts20190954 to X.W.) and the National Natural Science Foundation of China (42288201 to X.W.).

Author affiliations: [a]School of Life Sciences, The Chinese University of Hong Kong, Shatin, Hong Kong Special Administrative Region 999077, China; [b]School of Energy and Power Engineering, University of Shanghai for Science and Technology, Shanghai 200093, China; [c]Shandong Tianyu Museum of Nature, Shandong 273300, China; [d]College of Life Sciences, Linyi University, Shandong 276000, China; [e]Foundation for Scientific Advancement, Sierra Vista, AZ 85650; [f]Sustainable Energy and Environment Thrust, Hong Kong University of Science and Technology, Guangzhou 511458, China; [g]Department of Biology, Dakota State University, Madison, SD 57069; [h]David Geffen School of Medicine, University of California, Los Angeles, CA 90095; and [i]Department of Mechanical and Aerospace Engineering, The Hong Kong University of Science and Technology, Hong Kong Special Administrative Region 999077, China

1. T. N. Sullivan, M. A. Meyers, E. Arzt, Scaling of bird wings and feathers for efficient flight. *Sci. Adv.* **5**, eaat4269 (2019).
2. A. Azuma, *The Biokinetics of Flying and Swimming. AIAA Education Series* (American Institute of Aeronautics and Astronautics, Inc., Reston, VA, ed. 2, 2006), p. 518.
3. H. Tennekes, *The Simple Science of Flight: From Insects to Jumbo Jets* (MIT Press, Cambridge, MA, 2009), p. 152.
4. W. Shyy, H. Aono, C. Kang, H. Liu, *An Introduction to Flapping Wing Aerodynamics* (Cambridge University Press, Cambridge, UK, 2013), p. 297.
5. C. Hefler, C. K. Kang, H. Qiu, W. Shyy, *Distinct Aerodynamics of Insect-Scale Flight* (Cambridge University Press, Cambridge, UK, 2021).
6. C. J. Pennycuick, *Animal Flight* (The Institute of Biology's Studies in Biology, 1972), vol. 33, p. 64.
7. B. W. Tobalske, T. L. Hedrick, A. A. Biewener, Wing kinematics of avian flight across speeds. *J. Avian Biol.* **34**, 177–184 (2003).
8. W. Shyy, Y. S. Lian, J. Tang, D. Viieru, H. Liu, *Aerodynamics of Low Reynolds Number Flyers. Cambridge Aerospace Series* (Cambridge University Press, Cambridge, UK, 2007), p. 177.
9. D. D. Chin, D. Lentink, Flapping wing aerodynamics: From insects to vertebrates. *J. Exp. Biol.* **219**, 920–932 (2016).
10. Z. Hu, X. Y. Deng, Aerodynamic interaction between forewing and hindwing of a hovering dragonfly. *Acta Mech. Sin.* **30**, 787–799 (2015).
11. Y. S. Lian, T. Broering, K. Hord, R. Prater, The characterization of tandem and corrugated wings. *Prog. Aerosp. Sci.* **65**, 41–69 (2014).
12. R. Noda, X. Liu, C. Hefler, W. Shyy, H. H. Qiu, The interplay of kinematics and aerodynamics in multiple flight modes of a dragonfly. *J. Fluid Mech.* **967**, A31 (2023).
13. C. Hefler, R. Noda, H. H. Qiu, W. Shyy, Aerodynamic performance of a free-flying dragonfly–A span-resolved investigation. *Phys. Fluids* **32**, 041903 (2020).
14. C. Hefler, H. Qiu, W. Shyy, Aerodynamic characteristics along the wing span of a dragonfly *Pantala flavescens*. *J. Exp. Biol.* **221**, jeb171199 (2018).
15. X. T. Zheng *et al.*, Hind wings in basal birds and the evolution of leg feathers. *Science* **339**, 1309–1312 (2013).
16. X. Xu *et al.*, Four-winged dinosaurs from China. *Nature* **421**, 335–340 (2003).
17. Q. G. Li *et al.*, Reconstruction of *Microraptor* and the evolution of iridescent plumage. *Science* **335**, 1215–1219 (2012).
18. X. Xu, Z. Zhou, X. Wang, The smallest known non-avian theropod dinosaur. *Nature* **408**, 705–708 (2000).

19. J. Brougham, S. L. Brusatte, Distorted *Microraptor* specimen is not ideal for understanding the origin of avian flight. *Proc. Natl. Acad. Sci. U.S.A.* **107**, E155 (2010).
20. G. Dyke *et al.*, Aerodynamic performance of the feathered dinosaur *Microraptor* and the evolution of feathered flight. *Nat. Commun.* **4**, 2489 (2013).
21. C. Palmer, The aerodynamics of gliding flight and its application to the arboreal flight of the Chinese feathered dinosaur *Microraptor*. *Biol. J. Linn. Soc.* **113**, 828–835 (2014).
22. D. E. Alexander, E. P. Gong, L. D. Martin, D. A. Burnham, A. R. Falk, Model tests of gliding with different hindwing configurations in the four-winged dromaeosaurid *Microraptor gui*. *Proc. Natl. Acad. Sci. U.S.A.* **107**, 2972–2976 (2010).
23. S. Chatterjee, R. J. Templin, Biplane wing planform and flight performance of the feathered dinosaur *Microraptor gui*. *Proc. Natl. Acad. Sci. U.S.A.* **104**, 1576–1580 (2007).
24. D. Evangelista *et al.*, Aerodynamic characteristics of a feathered dinosaur measured using physical models: Effects of form on static stability and control effectiveness. *PLoS ONE* **9**, e85203 (2014).
25. A. R. Manafzadeh, K. Padian, ROM mapping of ligamentous constraints on avian hip mobility: Implications for extinct ornithodirans. *Proc. R. Soc. B. Biol. Sci.* **285**, 20180727 (2018).
26. M. A. R. Koehl, D. Evangelista, K. Yang, Using physical models to study the gliding performance of extinct animals. *Integr. Comp. Biol.* **51**, 1002–1018 (2011).
27. R. Pei *et al.*, Potential for powered flight neared by most close avialan relatives, but few crossed its thresholds. *Curr. Biol.* **30**, 4033–4046.e4038 (2020).
28. D. F. A. E. Voeten *et al.*, Wing bone geometry reveals active flight in Archaeopteryx. *Nat. Commun.* **9**, 923 (2018).
29. F. J. Serrano, L. M. Chiappe, Aerodynamic modelling of a Cretaceous bird reveals thermal soaring during avian evolution. *J. R. Soc. Interface.* **14**, 20170182 (2017).
30. F. J. Serrano *et al.*, "Laser-stimulated flourescence refines flight modelling of the early Cretacous bird Sapeornis" in *Pennaraptoran Theropod Dinosaurs: Past Progress and New Frontiers*, M. Pittman, X. Xu, Eds. (Bulletin of the American Museum of Natural History, New York, NY, 2020), vol. 420, pp. 333–344.
31. T. A. Dececchi, H. C. E. Larsson, M. Pittman, M. Habib, *High Flyer or High Fashion? A Comparison of Flight Potential among Small Bodied Paravians* (Bulletin of American Museum of Natural History, 2020), vol. 420.
32. T. A. Dececchi, H. C. E. Larrson, M. Pittman, M. B. Habib, "High flyer or high fashion? A comparison of flight potential among small bodied paravians" in *Pennaraptoran Dinosaurs: Past Progress and New Frontiers*, M. Pittman, X. Xu, Eds. (Bulletin of the American Museum of Natural History, New York, NY, 2020), pp. 295–320.
33. M. Pittman *et al.*, Exceptional preservation and foot structure reveal ecological transitions and lifestyles of early theropod flyers. *Nat. Commun.* **13**, 7684 (2022).
34. M. Pittman *et al.*, Preserved soft anatomy confirms shoulder-powered upstroke of early theropod flyers, reveals enhanced early pygostylian upstroke, and explains early sternum loss. *Proc. Natl. Acad. Sci. U.S.A.* **119**, e2205476119 (2022).
35. Y. Lian, T. Broering, K. Hord, R. Prater, The characterization of tandem and corrugated wings. *Prog. Aerosp. Sci.* **65**, 41–69 (2014).
36. F.-O. Lehmann, When wings touch wakes: Understanding locomotor force control by wake–wing interference in insect wings. *J. Exp. Biol.* **211**, 224–233 (2008).
37. S. J. Portugal *et al.*, Upwash exploitation and downwash avoidance by flap phasing in ibis formation flight. *Nature* **505**, 399–402 (2014).
38. F. Beaumont, S. Murer, F. Bogard, G. Polidori, Aerodynamic interaction of migratory birds in gliding flight. *Fluids* **8**, 50 (2023).
39. D. E. Alexander, Unusual phase relationships between the forewings and hindwings in flying dragonflies. *J. Exp. Biol.* **109**, 379–383 (1984).
40. E. Salami, T. A. Ward, E. Montazer, N. N. N. Ghazali, A review of aerodynamic studies on dragonfly flight. *Proc. Inst. Mech. Eng., Part C* **233**, 6519–6537 (2019).
41. J. Zhang, X. Y. Lu, Aerodynamic performance due to forewing and hindwing interaction in gliding dragonfly flight. *Phys. Rev. E* **80**, 017302 (2009).
42. Y. Luo, G. He, H. Liu, Q. Wang, H. Song, Aerodynamic performance of dragonfly forewing–hindwing interaction in gliding flight. *IOP Conf. Ser.: Mater. Sci. Eng.* **538**, 012048 (2019).
43. W. J. Maybury, F.-O. Lehmann, The fluid dynamics of flight control by kinematic phase lag variation between two robotic insect wings. *J. Exp. Biol.* **207**, 4707–4726 (2004).
44. J. R. Usherwood, F.-O. Lehmann, Phasing of dragonfly wings can improve aerodynamic efficiency by removing swirl. *J. R. Soc. Interface* **5**, 1303–1307 (2008).
45. D. Rival, D. Schönweitz, C. Tropea, Vortex interaction of tandem pitching and plunging plates: A two-dimensional model of hovering dragonfly-like flight. *Bioinspir. Biomim.* **6**, 016008 (2011).
46. C.-T. Hsieh, C.-F. Kung, C. C. Chang, C.-C. Chu, Unsteady aerodynamics of dragonfly using a simple wing–wing model from the perspective of a force decomposition. *J. Fluid Mech.* **663**, 233–252 (2010).
47. Z. Hu, X.-Y. Deng, Aerodynamic interaction between forewing and hindwing of a hovering dragonfly. *Acta Mech. Sin.* **30**, 787–799 (2014).
48. C.-M. Xie, W.-X. Huang, Vortex interactions between forewing and hindwing of dragonfly in hovering flight. *Theor. Appl. Mech. Lett.* **5**, 24–29 (2015).
49. ANSYS, *Fluent 2023 R1* (ANSYS, Canonsburg, PA, 2023).
50. T. G. Kaye *et al.*, Laser-stimulated fluorescence in paleontology. *PLoS ONE* **10**, e0125923 (2015).
51. M. Chotard *et al.*, New information on the hind limb feathering, soft tissues and skeleton of *Microraptor* (Theropoda: Dromaeosauridae). *BMC Ecol. Evol.* **25**, 37 (2025).
52. M. Grosmougin *et al.*, Forelimb feathering, soft tissues, and skeleton of the flying dromaeosaurid *Microraptor*. *BMC Ecol. Evol.* **25**, 65 (2025).
53. W. Shyy, P. Trizila, C. K. Kang, H. Aono, Can tip vortices enhance lift of a flapping wing? *AIAA J.* **47**, 289–293 (2009).
54. Z.-Y. Li, L.-H. Feng, T. Wang, Y. Liang, Lift generation mechanism of the leading-edge vortex for an unsteady plate. *J. Fluid Mech.* **972**, A30 (2023).
55. W. Shyy, H. Liu, Flapping wings and aerodynamic lift: The role of leading-edge vortices. *AIAA J.* **45**, 2817–2819 (2007).
56. C. P. Ellington, C. van den Berg, A. P. Willmott, A. L. R. Thomas, Leading-edge vortices in insect flight. *Nature* **384**, 626–630 (1996).
57. J. J. Videler, *Avian Flight* (Oxford University Press, 2006).
58. G. Sachs, Yaw stability in gliding birds. *J. Ornithol.* **146**, 191–199 (2005).
59. G. Han *et al.*, A new raptorial dinosaur with exceptionally long feathering provides insights into dromaeosaurid flight performance. *Nat. Commun.* **5**, 4382 (2014).
60. N. R. Longrich, J. Vinther, Q. Meng, Q. Li, A. P. Russell, Primitive wing feather arrangement in *Archaeopteryx lithographica* and *Anchiornis huxleyi*. *Curr. Biol.* **22**, 2262–2267 (2012).
61. N. Longrich, H. Tischlinger, C. Foth, "The feathers of the Jurassic Urvogel Archaeopteryx" in *The Evolution of Feathers*, C. Foth, O. W. M. Rauhut, Eds. (Springer, Cham, Switzerland, 2020), pp. 119–146.
62. C. Foth, H. Tischlinger, O. W. Rauhut, New specimen of *Archaeopteryx* provides insights into the evolution of pennaceous feathers. *Nature* **511**, 79–82 (2014).
63. T. A. Dececchi *et al.*, Aerodynamics show membrane-winged theropods were a poor gliding dead-end. *iScience* **23**, 10157 (2020).
64. C. Hefler, X. Liu, R. Noda, H. H. Qiu, W. Shyy, The interplay of kinematics and aerodynamics in multiple flight modes of a dragonfly. *J. Fluid Mech.* **967**, A31 (2023).
65. B. W. Tobalske, Aerodynamics of avian flight. *Curr. Biol.* **32**, R1105–R1109 (2022).
66. F. T. Muijres, L. C. Johansson, A. Hedenström, Leading edge vortex in a slow-flying passerine. *Biol. Lett.* **8**, 554–557 (2012).
67. J. J. Videler, E. J. Stamhuis, G. D. Povel, Leading-edge vortex lifts swifts. *Science* **306**, 1960–1962 (2004).
68. T. Y. Hubel, C. Tropea, The importance of leading edge vortices under simplified flapping flight conditions at the size scale of birds. *J. Exp. Biol.* **213**, 1930–1939 (2010).
69. W. Shyy *et al.*, Rigid and flexible low Reynolds number airfoils. *J. Aircr.* **36**, 523–529 (1999).
70. C. K. Kang, H. Aono, C. E. S. Cesnik, W. Shyy, Effects of flexibility on the aerodynamic performance of flapping wings. *J. Fluid Mech.* **689**, 32–74 (2011).
71. S. Wang *et al.*, Digital restoration of the pectoral girdles of two Early Cretaceous birds and implications for early-flight evolution. *eLife* **11**, e76086 (2022).
72. F. E. Novas *et al.*, Comments on the morphology of basal paravian shoulder girdle: New data based on unenlagiid theropods and paleognath birds. *Front. Earth Sci.* **9**, 662167 (2021).
73. C. Harvey, D. J. Inman, Gull dynamic pitch stability is controlled by wing morphing. *Proc. Natl. Acad. Sci. U.S.A.* **119**, e2204847119 (2022).
74. J. A. Cheney *et al.*, Raptor wing morphing with flight speed. *J. R. Soc. Interface* **18**, 20210349 (2021).
75. D. R. Warrick, M. W. Bundle, K. P. Dial, Bird maneuvering flight: Blurred bodies, clear heads. *Integr. Comp. Biol.* **42**, 141–148 (2002).
76. F. R. Menter, "Zonal two equation k-w turbulence models for aerodynamic flows" in *23rd Fluid Dynamics, Plasmadynamics, and Lasers Conference* (AIAA, Orlando, FL, 1993).
77. F. R. Menter, Two-equation eddy-viscosity turbulence models for engineering applications. *AIAA J.* **32**, 1598–1605 (1994).
78. ANSYS, *Workbench 2023 R1* (ANSYS, Canonsburg, PA, 2023).
79. P. G. Falkowski *et al.*, The rise of oxygen over the past 205 million years and the evolution of large placental mammals. *Science* **309**, 2202–2204 (2005).
80. P. Ward, R. Berner, G. Dyke, G. Kaiser, *Why Were There Dinosaurs? Why Are There Birds. Living Dinosaurs* (Wiley-Blackwell, Hoboken, NJ, 2011), pp. 30–38.
81. I. J. Glasspool, A. C. Scott, Phanerozoic concentrations of atmospheric oxygen reconstructed from sedimentary charcoal. *Nat. Geosci.* **3**, 627–630 (2010).
82. G. J. Retallack, Greenhouse crises of the past 300 million years. *Bull. Geol. Soc. Am.* **121**, 1441–1455 (2009).
83. F. J. Serrano *et al.*, The effect of long-term atmospheric changes on the macroevolution of birds. *Gondwana Res.* **65**, 86–96 (2019).
84. X. L. Wang *et al.*, Basal paravian functional anatomy illuminated by high-detail body outline. *Nat. Commun.* **8**, 14576 (2017).